

RESEARCH ARTICLE

10.1002/2017JD027061

Key Points:

- Variations of reactive nitrogen (NO_y) and source gas N_2O show coherent QBO signals in the tropical stratosphere
- Nitrogen species measured by the Aura MLS and Odin OSIRIS satellite instruments show consistent interannual variability
- Total NO_y budget and its variability obtained from the WACCM4 simulations agree with the satellite measurements

Supporting Information:

- Supporting Information S1

Correspondence to:

M. Park,
mjeoeng@ucar.edu

Citation:

Park, M., Randel, W. J., Kinnison, D. E., Bourassa, A. E., Degenstein, D. A., Roth, C. Z., ... Santee, M. L. (2017). Variability of stratospheric reactive nitrogen and ozone related to the QBO. *Journal of Geophysical Research: Atmospheres*, 122, https://doi.org/10.1002/2017JD027061

Received 1 MAY 2017

Accepted 29 AUG 2017

Accepted article online 31 AUG 2017

Variability of Stratospheric Reactive Nitrogen and Ozone Related to the QBO

M. Park¹ , W. J. Randel¹ , D. E. Kinnison¹ , A. E. Bourassa² , D. A. Degenstein², C. Z. Roth², C. A. McLinden³ , C. E. Sioris³ , N. J. Livesey⁴ , and M. L. Santee⁴ 

¹National Center for Atmospheric Research, Boulder, CO, USA, ²Institute of Space and Atmospheric Studies, University of Saskatchewan, Saskatoon, Saskatchewan, Canada, ³Air Quality Research Division, Environment and Climate Change Canada, Toronto, Ontario, Canada, ⁴Jet Propulsion Laboratory, Pasadena, CA, USA

Abstract The stratospheric quasi-biennial oscillation (QBO) dominates interannual variability of dynamical variables and trace constituents in the tropical stratosphere and provides a natural experiment to test circulation-chemistry interactions. This work quantifies the relationships among ozone (O_3), reactive nitrogen (NO_y), and source gas N_2O , and their links to the QBO, based on satellite constituent measurements and meteorological data spanning 2005–2014 (over four QBO cycles). Data include O_3 , HNO_3 , and N_2O from the Aura Microwave Limb Sounder and an NO_x proxy derived from Optical Spectrograph and Infrared Imager System NO_2 measurements combined with a photochemical box model (= NO_x^*). Results are compared to simulations from the Whole Atmosphere Community Climate Model, version 4 incorporating a QBO circulation nudged to assimilated winds. Cross correlations and composites with respect to the QBO phase show coherent 180° out-of-phase relationships between NO_y and N_2O throughout the stratosphere, with the NO_x/HNO_3 ratio increasing with altitude. The anomalies in NO_y species propagate coherently downward with the QBO. Ozone is anticorrelated with reactive nitrogen in the middle stratosphere above ~28 km due to NO_x control of ozone catalytic loss cycles. Quantitative comparisons of nitrogen partitioning and O_3 sensitivity to NO_x show good overall agreement between satellite observations and model results (suggesting closure of the NO_y budget), although the model results show larger (up to ~20%) N_2O , NO_x , and O_3 variations near ~35 km compared to observations. These analyses serve to assess the consistency of diverse satellite-based data sets and also to evaluate nitrogen partitioning and NO_x -dependent ozone chemistry in the global model.

1. Introduction

The stratospheric quasi-biennial oscillation (QBO) dominates the interannual variability in the tropical stratosphere for zonal winds, temperatures, meridional circulation, and trace species (Baldwin et al., 2001, and references therein). Tropical stratospheric ozone (O_3) exhibits a strong QBO signal, evident as variations in the lower stratosphere (tied to transport) and in the middle and upper stratosphere (from QBO-induced changes in chemical loss rates). These separate influences have been deduced from observations and modeling studies (e.g., Chipperfield & Gray, 1992; Chipperfield et al., 1994; Gray & Chipperfield, 1990; Gray & Pyle, 1989; Randel & Wu, 1996; Schoeberl et al., 2008; Zawodny & McCormick, 1991) and are tied to the long photochemical lifetime (dynamical control) for ozone in the lower stratosphere in contrast to short lifetime (chemical control) in the middle and upper stratosphere (e.g., Chipperfield & Gray, 1992). An important aspect of these studies is the influence of reactive nitrogen species (NO_y), which is defined as the sum of nitrogen oxides (NO and NO_2 , collectively, NO_x) and all the reservoir species, on the ozone QBO in the middle stratosphere; this $\text{O}_3\text{-NO}_y$ coupling has also been highlighted in the context of decadal trends by Nedoluha et al. (2015). The key catalytic cycles controlling ozone loss in this altitude region are linked to reactive nitrogen, in the form of nitrogen oxides. Several studies have analyzed the ozone QBO in chemistry-transport or chemistry-climate models (Bruhwiler & Hamilton, 1999; Butchart et al., 2003; Nagashima et al., 1998; Punge & Giorgetta, 2008; Tian et al., 2006), showing overall similar behavior to earlier idealized modeling studies in terms of dynamical and chemical responses, including the important influence of NO_y (although Butchart et al., 2003, do not consider NO_y changes in their simulation).

This study is motivated by the availability of long records of ozone and reactive nitrogen species (and the source gas, N_2O) from satellite measurements now spanning over a decade, which can be used to quantitatively evaluate observed QBO behavior. These species include O_3 , nitrous oxide (N_2O), and nitric acid (HNO_3) from the Aura Microwave Limb Sounder (MLS) spanning 2004 to present (Waters et al., 2006) and O_3 and

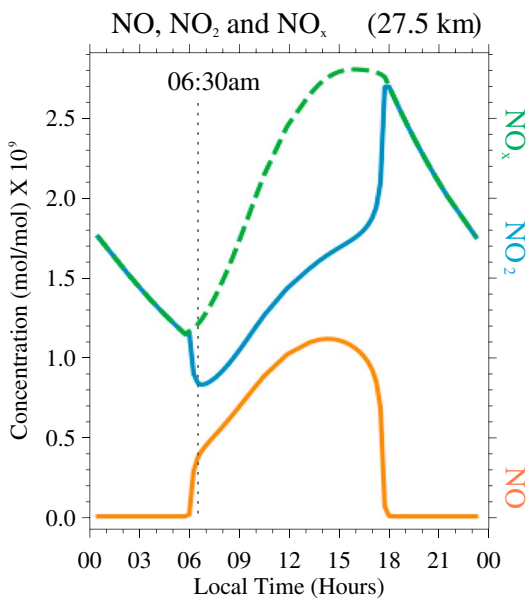


Figure 1. Diurnal cycles of NO, NO₂, and NO_x (= NO + NO₂) at the equator and 27.5 km derived from the photochemical box model. OSIRIS retrievals of NO₂ in the early morning (06:30 LST) constrain the box model to provide daily average NO_x*.

et al., 2012). OSIRIS is composed of two independent components, the grating Optical Spectrograph (OS), which measures spectra over the 280–800 nm range, and the three-channel Infrared Imager (IRI), which observes both scattered sunlight and the airglow emissions at 1.26, 1.27, and 1.53 μ m (Degenstein et al., 2003). OSIRIS measurements of limb-scattered sunlight in the near-UV, visible, and near-IR regions have been used to derive near-global vertical profiles of O₃, bromine monoxide (BrO), aerosols, and NO₂. The equator crossing time of the Odin satellite is close to 06:30 local solar time (LST) for the descending orbit and 18:30 for the ascending orbit, respectively, which provides continuous measurements on the daytime orbit. The limb-scattering measurements are only available for the sunlit portion of the atmosphere and do not cover polar night (the available sampling is shown by Adams et al., 2014). OSIRIS O₃ is retrieved using the Multiplicative Algebraic Reconstruction Technique (MART) and has vertical resolution of 1.5 km between 10 and 60 km. Details of OSIRIS O₃ retrievals are presented in Degenstein et al. (2009).

There are several separate NO₂ retrievals that have been derived from OSIRIS data. The so-called v3.0 NO₂ product is described by Brohede et al. (2007), who used an Optimum Estimation retrieval based on a spectral fit at 36 measured wavelengths. Bourassa et al. (2011) developed a fast NO₂ retrieval based on a small number of wavelengths incorporated in a MART retrieval. Direct comparison between the MART NO₂ and the v3.0 NO₂ product shows qualitative agreement, with percent difference less than 10% near the peak of the NO₂ number density profiles (Bourassa et al., 2011). Altitude range of NO₂ retrievals depends on the data quality at the lower and upper limits of the retrieval. The v6 product is reported on altitude grids from the cloud top or 8.5 km, whichever is lower, up to 49.5 km with a vertical resolution of 2 km. Most profiles extend up to ~40.5 km. The OSIRIS v6 NO₂, which is used in this study, has a bias of ~10% or less between ~14 and 37 km (Sioris et al., 2017).

OSIRIS measurements are used to derive NO₂ number density profiles, based on observations during descending portions of the orbit (near 06:30 A.M. LST). Nitrogen oxides (NO and NO₂) are in rapid photochemical equilibrium, undergoing strong diurnal variations during the day, and the diurnal cycle of NO_x (= NO + NO₂) depends on their sum (e.g., Brasseur & Solomon, 2005). This behavior is illustrated in Figure 1 based on the photochemical box model outputs. To make comparisons of satellite observations with the model outputs without the influence of the diurnal cycle of NO₂, we constructed daily mean mixing ratios of NO_x based on a comprehensive photochemical box model (Adams et al., 2017; McLinden et al., 2000; Prather, 1992).

nitrogen dioxide (NO₂) measured by the Optical Spectrograph and Infrared Imager System (OSIRIS) instrument (Haley et al., 2004) on the Odin satellite (Murtagh et al., 2002) covering from 2002 to present. The OSIRIS NO₂ data set used here is relatively new, and one of our goals is to evaluate its geophysical and temporal variability. With these combined data sets, we focus on a quantitative evaluation of the reactive nitrogen budget and its links to ozone through the QBO cycle in the stratosphere. Our objective is to quantify the QBO variations and interrelationships among those species from observational data for the period 2005–2014, covering over four complete QBO cycles. We furthermore compare the satellite observations with outputs from a state-of-the-art chemistry-climate model (Whole Atmosphere Community Climate Model, version 4, WACCM4) (see Marsh et al., 2013), to evaluate the model behavior and aid interpretation of observations from the combined satellite measurements. Because the QBO dominates the tropical interannual variability for all of the species in both the measurements and the model, these comparisons provide a stringent test of both model and data in a complex yet realistic context. Our analysis of QBO-related variabilities is a complement to evaluations of time-averaged behavior of the stratospheric reactive nitrogen budget, such as from Brohede et al. (2008) and Sheese et al. (2006).

2. Data and Analyses

2.1. OSIRIS

The OSIRIS on board the Odin spacecraft was launched on 20 February 2001 into a low-Earth, Sun-synchronous orbit (Llewellyn et al., 2004; McLinden et al., 2012).

The model has been updated to include newer reactions, rate constants, and absorption cross sections (see Adams et al., 2017). OSIRIS NO₂ is used as the basis to estimate NO (and hence NO_x) (see equation (1) below). Time adjustment was applied to the OSIRIS NO₂ profiles so that the measurements represent 06:30 A.M. LST. The photochemical box model is then applied to each NO₂ number density profile to estimate the diurnal cycle in NO and NO₂ (as illustrated in Figure 1). These are then used to calculate a daily average value for the NO_x proxy (hereafter NO_x*).

$$[\text{NO}_x^*] = [\text{NO}_2]_{\text{OSIRIS}, 06:30} \left\{ \frac{[\text{NO}_x]_{\text{daily}}}{[\text{NO}_2]_{06:30}} \right\}_{\text{model}} \quad (1)$$

NO_x* number densities are converted to mixing ratios using temperature (*T*) and pressure (*p*) from the European Centre for Medium-Range Weather Forecasting (ECMWF) meteorological analyses, which are used in the OSIRIS NO₂ retrievals and provided with the individual OSIRIS profiles. The box model includes input of OSIRIS ozone and aerosol extinction, as well as the retrieved surface reflectance and *T* and *p* from ECMWF. We note that similar methods were used in calculating a NO_y proxy, which includes O₃, NO₂, and HNO₃ measurements from Odin satellite in Brohede et al. (2008). A comparison of the Odin NO_y proxy with a climatology from the Atmospheric Chemistry Experiment-Fourier Transform Spectrometer (ACE-FTS) is presented in Jones et al. (2011). We note that the NO_x proxy we have derived from OSIRIS has not been utilized previously.

OSIRIS daily NO_x and O₃ profiles are used to construct daily gridded data on 10° latitude × 20° longitude grids and are averaged on a monthly timescale. The retrievals are available on an oversampled vertical grid of ~1 km from 10.5–59.5 km for OSIRIS O₃ and 10.5–39.5 km for NO₂ and NO_x*.

2.2. MLS

The Earth Observing System (EOS) Microwave Limb Sounder (MLS) on board the Aura spacecraft measures thermal emission from the limb of Earth's atmosphere. The MLS instrument provides daily global [82°S–82°N] measurements of vertical profiles of temperature and chemical constituents from the upper troposphere to the mesosphere (Waters et al., 2006). The MLS v4.2 data, which are used in this study, are the fourth "public release" and include (among other improvements) updates to spectroscopy and instrument calibration knowledge compared to the previous versions (Livesey et al., 2017). We utilize MLS v4.2 O₃, HNO₃, and N₂O for the period from 2005 to 2014. Individual profiles are quality screened as described by Livesey et al. (2017).

The MLS v4.2 O₃ product is retrieved using 240 GHz radiances. The vertical resolution of O₃ varies with pressure, ranging from 2.5 to 3.5 km over the 316 to 1 hPa domain. Precision and accuracy of individual profiles of O₃ vary with altitude and both are better than 10% in the 68–1 hPa pressure range (Livesey et al., 2017). Detailed validation of the MLS O₃ product based on the v2.2 retrieval was previously reported by Froidevaux et al. (2008) and Livesey et al. (2008).

The standard MLS HNO₃ product is taken from the 240 GHz radiometer at pressures equal to or greater than 22 hPa and from the 190 GHz radiometer for pressures less than 15 hPa. The vertical resolution of the v4.2 HNO₃ is 3–4 km through most of the stratosphere. Precision on individual profiles is ±0.6 ppbv over most of the stratosphere, increasing to 1.2 ppbv at 1.5 hPa and smaller pressures, and estimated uncertainty varies from ±0.5 to ±2 ppbv (or approximately ±10%) (Livesey et al., 2017). The detailed validation of the v2.2 HNO₃ products is presented by Santee et al. (2007).

The standard product for MLS v4.2 N₂O is obtained from the 190 GHz radiances instead of the 640 GHz retrievals, as used in previous versions, due to degradation of the band measuring of the latter. The resolution and precision of the 190 GHz N₂O data are slightly worse than those of the 640 GHz retrievals (Livesey et al., 2017). The recommended pressure range of the 190 GHz N₂O data is 68–0.46 hPa, and the vertical resolution is 4–8 km. Estimated precision on a single profile varies from ~15 to 20 ppbv. Detailed validation of v2.2 N₂O is presented in Lambert et al. (2007).

MLS O₃, HNO₃, and N₂O are gridded on 7.5° latitude × 15° longitude grids and averaged in time to construct monthly averages on each pressure level. Our analyses throughout the paper are performed on the standard MLS pressure grid, with six equally spaced levels per decade of pressure for HNO₃ and N₂O (vertical sampling of ~2.7 km) and twelve for O₃.

Monthly mean gridded data are used to make zonal mean tropical averages for both OSIRIS and MLS and specific latitudes ranges are noted in each figure.

2.3. WACCM4

The Community Earth System Model version 1 (CESM1), Whole Atmosphere Community Climate Model (WACCM), is a coupled chemistry-climate model from the Earth's surface to the lower thermosphere (Marsh et al., 2013, and the references within). WACCM is superset of the Community Atmosphere Model, version 4 (CAM4), and includes all of the physical parameterizations of CAM4 (Neale et al., 2013) and a finite volume dynamical core (Lin, 2004) for tracer advection. The WACCM4 simulation used in this study is run with specified dynamics (SD) fields (Lamarque et al., 2012), using meteorological analyses from the National Aeronautics and Space Administration (NASA) Global Modeling and Assimilation Office (GMAO) Modern-Era Retrospective Analysis for Research and Applications (MERRA) (Rienecker et al., 2011) for the period from January 2005 to December 2014. Hence, the QBO circulation in the model is synchronized with that in the real atmosphere. The horizontal resolution of the model is 1.9° latitude $\times 2.5^\circ$ longitude, and the model has 88 vertical levels from the surface up to about 150 km. The vertical resolution in the lower stratosphere ranges from ~ 1 km near the tropopause to about 2 km near the stratopause. The simulation used in this work is based on the REF-C1SD scenario as defined by the International Global Atmospheric Chemistry/Stratosphere-troposphere Processes and their Role in Climate (IGAC/SPARC) Chemistry-Climate Model Initiative (CCMI) (Morgenstern et al., 2017). This version of WACCM4 contains a detailed representation of tropospheric and stratospheric chemistry (Kinnison et al., 2007; Lamarque et al., 2012; Tilmes et al., 2016). The species included within this mechanism are contained within the O_x , NO_x , HO_x , ClO_x , and BrO_x chemical families, along with methane (CH_4) and its degradation products. In addition, 20 primary nonmethane hydrocarbons and related oxygenated organic compounds are represented along with their surface emissions. There are a total of 183 species and 472 chemical reactions; this includes 17 heterogeneous reactions on multiple aerosol types (i.e., sulfate, nitric acid trihydrate, and water ice). The nitrogen chemistry specific to this work includes the following species: N , NO , NO_2 , NO_3 , N_2O_5 , HNO_3 , HO_2NO_2 , $ClONO_2$, and $BrONO_2$. Reaction rate constants are from the NASA JPL-2010 recommendations (Sander et al., 2011).

We use temperature from the National Centers for Environmental Prediction/National Center for Atmospheric Research (NCEP/NCAR) reanalysis (Kistler et al., 2001) to calculate thermal tropopause height. Additionally, equatorial zonal wind observations over Singapore (Naujokat, 1986) and monthly averaged zonal mean zonal winds from the ECMWF Interim reanalysis (ERA-Interim) data (Dee et al., 2011) are used to quantify dynamical variability of the QBO in combination with observations. For WACCM4, zonal mean winds from MERRA are shown, because MERRA winds were used to nudge the model dynamics. The dynamical variability of the QBO in ERA-Interim and MERRA are generally consistent (figures not shown). For all of the satellite data, model outputs, and QBO winds, we examine deseasonalized anomalies after subtracting the mean seasonal cycle which is defined by averages over 2005–2014 for each month.

2.4. Nitrogen Partitioning

The primary source of stratospheric reactive nitrogen (NO_y) is oxidation of N_2O transported from the troposphere. NO_y plays an important role in stratospheric chemistry by contributing to ozone destruction via the NO_x catalytic cycle and by influencing partitioning of other reactive compounds in the stratosphere (e.g., Crutzen, 1971; McElroy & McConnell, 1971). Partitioning of NO_y species is determined by local photochemical balances, which have strong dependency on season and altitude. The full detailed partitioning of NO_y involves numerous species, but the primary components in the stratosphere are NO , NO_2 , HNO_3 , N_2O_5 , and $ClONO_2$ (the so-called “big five”) (Brohede et al., 2008). Figure 2a shows the time-averaged vertical profiles of these species along with total NO_y in the tropics ($10^\circ S$ – $10^\circ N$) obtained from WACCM4. The total NO_y budget in most of the tropical stratosphere is accounted for mainly by NO , NO_2 (collectively NO_x), and HNO_3 ($\sim 90\%$ of the total NO_y between 100 and 1 hPa). HNO_3 is the largest component at pressures greater than ~ 10 hPa, while the fraction of NO_x increases with altitude and explains most of the total NO_y budget at pressures smaller than ~ 10 hPa. Vertical profiles of time-averaged N_2O show nearly constant values in the troposphere, and N_2O starts decreasing in the stratosphere. Note that only a small fraction (less than 10%) of N_2O is converted into NO_y , as the majority of N_2O is destroyed by photolysis to produce N_2 (i.e.,

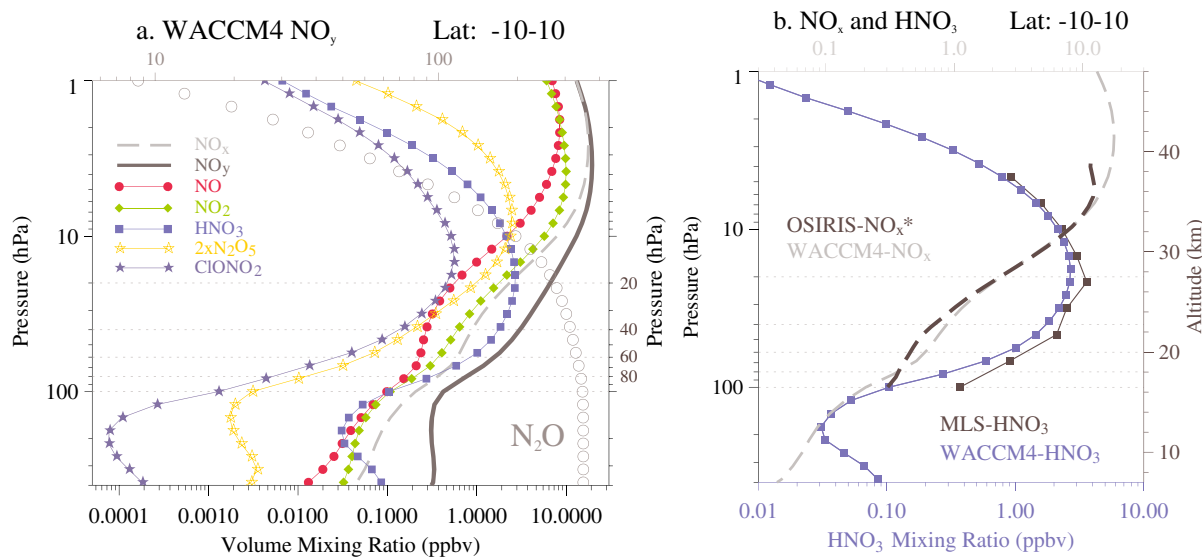


Figure 2. (a) Vertical profiles of time-averaged NO_y (solid gray line), primary component species (so-called big five: NO, NO₂, HNO₃, 2 × N₂O₅, and ClONO₂) and N₂O (open circles) derived from WACCM4 climatology. (b) Time-averaged NO_x and HNO₃ from WACCM4 versus OSIRIS NO_x* and MLS HNO₃ climatologies averaged between 10°S and 10°N latitude.

$N_2O + h\nu = > N_2 + O(^1D)$ (Brasseur & Solomon, 2005; chapter 6, SPARC, 2010). The results in Figure 2a show close agreement to the result from a photochemical box model from Brohede et al. (2008); see their Figure 1.

Figure 2b shows vertical profiles of time-averaged MLS HNO₃ and OSIRIS NO_x* compared with the respective WACCM4 results. The vertical profiles show the change in nitrogen partitioning from the lower to the upper stratosphere (from HNO₃ to NO_x dominance), with consistent behavior between the model and satellite data. Differences between WACCM4 NO_x and OSIRIS NO_x* are within ±10% over ~26–34 km and increase above and below this range. The time-averaged vertical profile of HNO₃ from MLS has higher mixing ratios (~10–15% difference) with respect to WACCM4 over 31.6–6.8 hPa, with larger differences (up to ~40%) at 21.5, 46, and 68 hPa.

3. Results

3.1. QBO Variability in O₃ and Nitrogen Species

The primary driver for the QBO variability in O₃ and other tracers is transport by the balanced secondary meridional circulation tied to the transient zonal wind and temperature fields (Baldwin et al., 2001; Bruhwiler & Hamilton, 1999; Chipperfield & Gray, 1992; Fleming et al., 2002; Punge & Giorgetta, 2008; Randel & Wu, 1996; Tian et al., 2006; Witte et al., 2008). In the tropical lower stratosphere, where the chemical lifetime of O₃ is relatively long and the vertical gradient is strong, variability in O₃ is largely determined by transport. In the upper stratosphere, above ~28 km, variability in O₃ is affected by both transport and photochemistry. Figure 3 illustrates the observed time variations of O₃, NO_x*, and HNO₃ along with MLS N₂O in the tropical middle stratosphere (10 hPa, ≈32 km) during 2005–2014. In Figure 3, O₃ is shown based on both MLS and OSIRIS data, revealing excellent agreement (consistent with the comparisons shown in Tegtmeier et al., 2013). Hereafter, we focus on the MLS O₃ results, although very similar behavior is found for OSIRIS O₃.

The dominant variability in all of the constituents shown in Figure 3 is tied to the QBO. Interannual variations of NO_x* and HNO₃ are in phase with each other, and 180° out of phase with N₂O and O₃. The coherent variations between NO_x* and HNO₃ and their strong negative correlations with N₂O result from N₂O being the major source of NO_y species. As the source (N₂O and also O(^1D)) is modulated by the QBO circulation, the variations in vertical transport influence the degree of N₂O oxidation and the mixing ratios of HNO₃ and NO_x*. The strong negative correlation between O₃ and NO_x* is a result of NO_x being the primary sink of O₃ in the middle stratosphere (Salawitch et al., 2005).

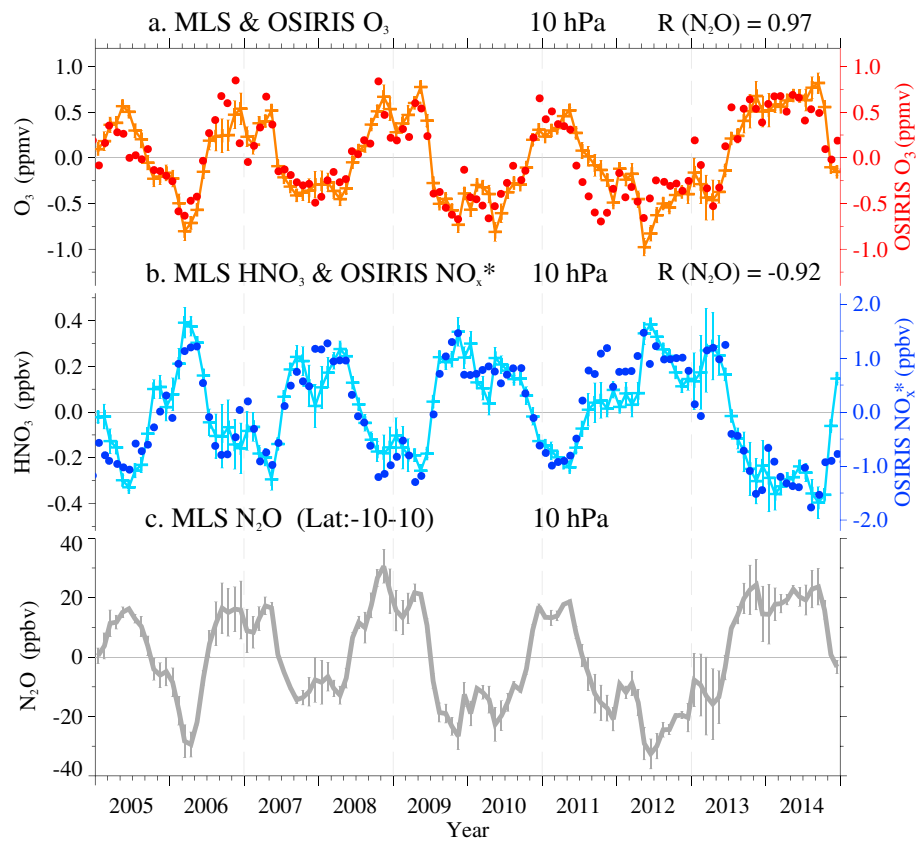


Figure 3. Time series of monthly mean anomalies at 10 hPa averaged between 10°S and 10°N of (a) O_3 from MLS (orange crosses) and OSIRIS (red solid dots), (b) HNO_3 from MLS (light blue crosses) and NO_x^* from OSIRIS (blue solid dots), and (c) N_2O from MLS. Note the different vertical scales for HNO_3 and NO_x^* . Thin solid gray lines in Figure 3c represent 1 sigma standard deviation of MLS N_2O monthly mean anomalies. Correlation coefficients between MLS N_2O and O_3 (and HNO_3) are shown in Figure 3a (and Figure 3b).

The vertical structure of interannual variations of O_3 anomalies is highlighted in Figure 4a, which shows monthly mean equatorial zonal winds superimposed on monthly anomalies of MLS O_3 . Positive and negative O_3 anomalies coexist with westerly and easterly zonal wind shear zones tied to the QBO in the lower stratosphere (pressures greater than ~ 15 hPa). These O_3 anomalies occur as a result of variations in vertical transport associated with the QBO meridional circulation, as illustrated in Figure 2 of Gray and Chipperfield (1990). Monthly anomalies of O_3 at higher altitude (pressures less than ~ 15 hPa) show the opposite phase relationship with zonal winds compared to those at lower altitudes. For comparison, monthly anomalies of O_3 from WACCM4 averaged over the same latitude region are shown in Figure 4b. Variability of WACCM4 O_3 agrees remarkably well with that of MLS O_3 (Figure 4a) in most details, except that the magnitude of WACCM4 O_3 anomalies is $\sim 20\%$ larger than that of MLS O_3 at altitudes above ~ 10 hPa. Similar behavior is found with comparisons to OSIRIS O_3 (figures not shown).

Interannual variations of OSIRIS NO_x^* anomalies are shown in Figure 5a, compared to WACCM NO_x anomalies in Figure 5b. The OSIRIS NO_x^* shows strong QBO variations at altitudes above ~ 27 km (~ 20 hPa) that descend in a coherent manner with the QBO circulation. Excellent overall agreement is seen with the NO_x patterns from the WACCM4 simulation (correlations between the two data sets are ~ 0.65 to 0.85 over pressure levels from 46 to 6.8 hPa), although the magnitudes of the WACCM4 NO_x anomalies are larger than those from the OSIRIS data at ~ 20 hPa pressure level and above.

In Figure 6, we show tracer-tracer correlations from both the satellite data and the WACCM4 simulations, providing a tool for diagnosing relationships among multiple species. Equatorial anomalies of MLS O_3 , HNO_3 , and OSIRIS NO_x^* versus MLS N_2O at 10 hPa are shown in Figure 6a. Consistent with the time series in Figure 3, Figure 6a shows strong negative correlations between reactive nitrogen species (NO_x and HNO_3)

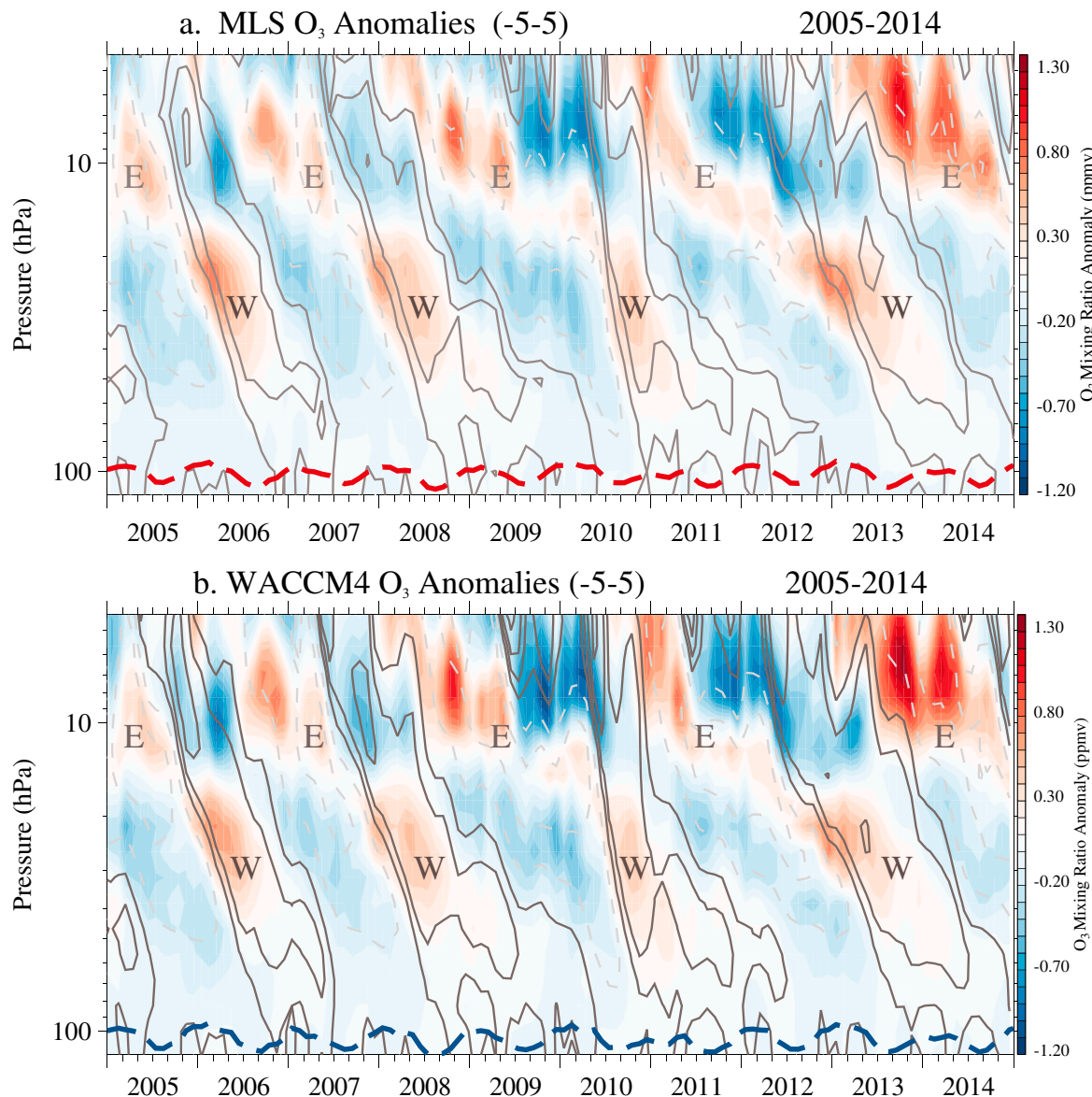


Figure 4. Time versus altitude sections of monthly mean anomalies of O₃ (unit: ppmv) from (a) MLS and (b) WACCM4 averaged between 5°S and 5°N for 2005–2014. Monthly averaged zonal mean zonal winds (unit: m s⁻¹) from (a) ERA-Interim and (b) WACCM4 are overlaid as solid gray lines (W and E represent westerly and easterly winds, respectively). Red and blue dashed lines denote thermal tropopause height calculated from NCEP/NCAR reanalysis (Figure 4a) and WACCM4 (Figure 4b) temperature profiles.

and N₂O and positive correlations between O₃ and N₂O. Both observations (Figure 6a) and the model results (Figure 6b) show compact relationships with similar slopes. At 10 hPa the (NO_x/N₂O) slope is steeper than the (HNO₃/N₂O) slope, but the slopes relative to N₂O depend on altitude (as quantified below). For HNO₃ the scatter and slope versus N₂O are similar between the observations and the model, while for NO_x the observations show slightly more scatter than the model.

Similar tracer-tracer correlations at 21 hPa are shown in Figures 6c and 6d, revealing anticorrelations for NO_x and HNO₃, with larger scatter in the satellite data for the relatively small NO_x* values. Positive O₃-NO_x correlation is found at 21 hPa, as this is in the region where O₃ is under dynamical control. Overall, the behaviors of O₃ and reactive nitrogen species in relation to N₂O are remarkably similar between the observations and model.

As shown in Figure 6, the relationships among the various species relative to N₂O change as a function of altitude. Negative correlations between N₂O and NO_y are expected throughout the stratosphere since the

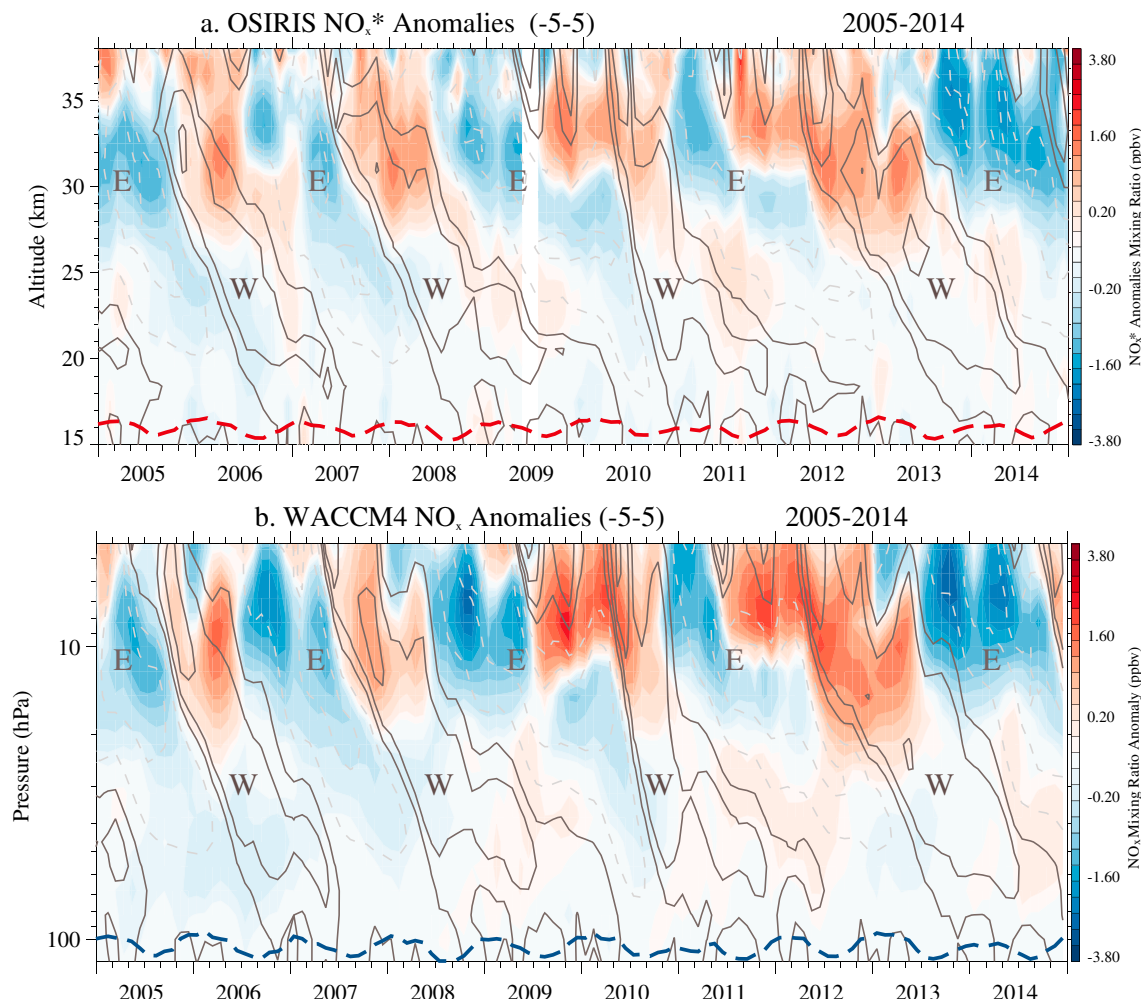


Figure 5. Time versus altitude sections of monthly mean anomalies of (a) OSIRIS NO_x^* (unit: ppbv) and (b) WACCM4 NO_x averaged between 5°S and 5°N for 2005–2014. Equatorial zonal winds and tropopause heights are included as in Figure 4.

reaction of $\text{N}_2\text{O} + \text{O}^1\text{D}$ is the source of NO_y . For the range of variability studied here, a linear anticorrelation between NO_y and N_2O is expected, whereas from a global perspective the NO_y - N_2O relationship can have curvature due to NO_y loss processes in the upper stratosphere (see discussion of NO_y - N_2O curvature in Figure 6.14 of SPARC, 2010). The linear behavior for the QBO situation is confirmed in Figure 7a, which shows strong anticorrelation between N_2O and $\text{HNO}_3 + \text{NO}_x$, a proxy for NO_y , throughout the stratosphere. The correlations from observations (MLS HNO_3 and OSIRIS NO_x^* combined) are in good agreement with WACCM4 results for pressure levels from 46 to 10 hPa. Figure 7b shows correlation coefficients between O_3 and the NO_y proxy from satellite data and from WACCM4. There are strong positive correlations below ~ 28 km and negative correlations above, consistent with the change from dynamical control to photochemical control of ozone across this level. Correlation coefficients from satellite data decrease at pressures less than ~ 10 hPa both in Figures 7a and 7b, which might imply lower NO_x^* data quality at higher levels.

3.2. Composed QBO Constituent Variability

Previous satellite measurements have shown that QBO variations in O_3 are closely tied to those in NO_y species (Hauchecorne et al., 2010; Kyrölä et al., 2010). In this section, we explore variations in O_3 , N_2O , HNO_3 , and NO_x in terms of their specific phasing with respect to QBO winds. As discussed above, monthly anomalies of O_3 from MLS and WACCM4 show consistent QBO structure with similar amplitude and phase (Figure 4). Here we quantify this behavior by compositing monthly anomalies of chemical constituents

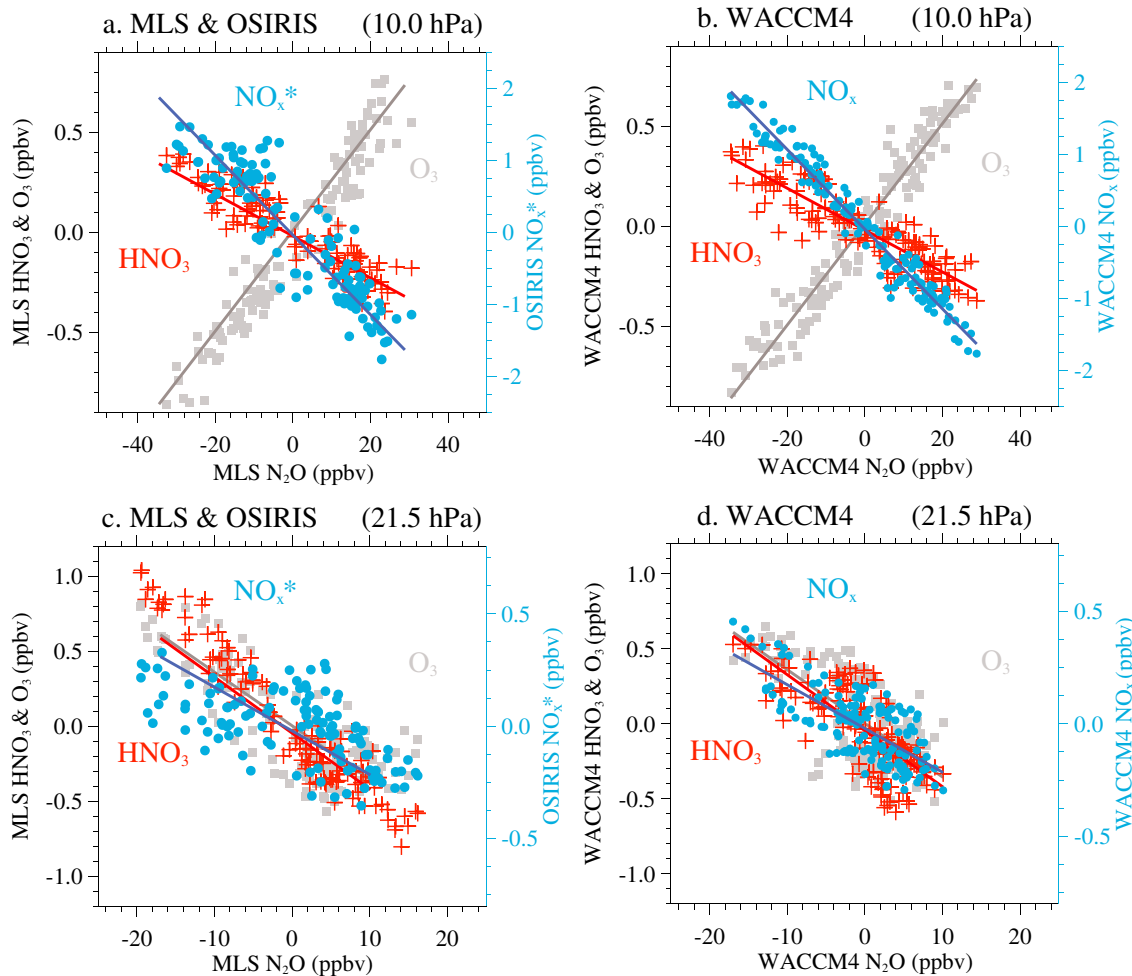


Figure 6. Scatterplots of monthly mean anomalies of N₂O versus O₃ (gray squares), N₂O versus HNO₃ (red crosses), and N₂O versus NO_x (blue dots) averaged between 10°S and 10°N from (a and c) MLS (O₃, HNO₃, and N₂O) and OSIRIS (NO_x* and (b and d) WACCM4 at 10 hPa (Figures 6a and 6b) and 21 hPa (Figures 6c and 6d). Solid lines show least squares fits estimated from WACCM4 in Figures 6b and 6d and overplotted in Figures 6a and 6c.

with respect to the phase of the QBO. The composite averages are constructed based on the timing of the onset of westerly winds at 20 hPa as previously done by Hommel et al. (2015). Specifically, monthly anomalies of chemical constituents at all altitudes are calculated in a time lag coordinate with respect to near-zero zonal winds at 20 hPa. This is to focus on a relationship between the QBO winds and the chemical constituents through an average QBO cycle. We combined the four QBO cycles spanning 2005–2014 following this method and made composite averages of separate chemical species from MLS, OSIRIS, and WACCM4.

Figure 8a shows the QBO composite average of equatorial O₃ anomalies (5°S–5°N) from MLS. Positive (negative) O₃ anomalies propagate downward in a coherent manner with westerly (easterly) wind shears between ~15 and 70 hPa, where vertical transport induced by the QBO is acting on the vertical gradients of O₃. Above this altitude ($p < \sim 15$ hPa), the phase of O₃ anomalies with respect to QBO winds is reversed mainly due to chemical control by NO_x. A similar composite average of O₃ anomalies from WACCM4 (Figure 8b) shows overall agreement with MLS, although at higher altitudes ($p < \sim 15$ hPa), WACCM4 O₃ anomalies show relatively larger amplitudes (up to ~20% difference) than those of MLS O₃ (as noted previously).

QBO composite averages for individual components of reactive nitrogen (NO_y) are presented in Figure 9, including NO_x, HNO₃, and N₂O from both observations and WACCM4 results. All of the species show coherent downward propagating features associated with the progression of the QBO. The variations in HNO₃ and NO_x are out of phase with respect to those of N₂O due to chemical production and loss (as seen in

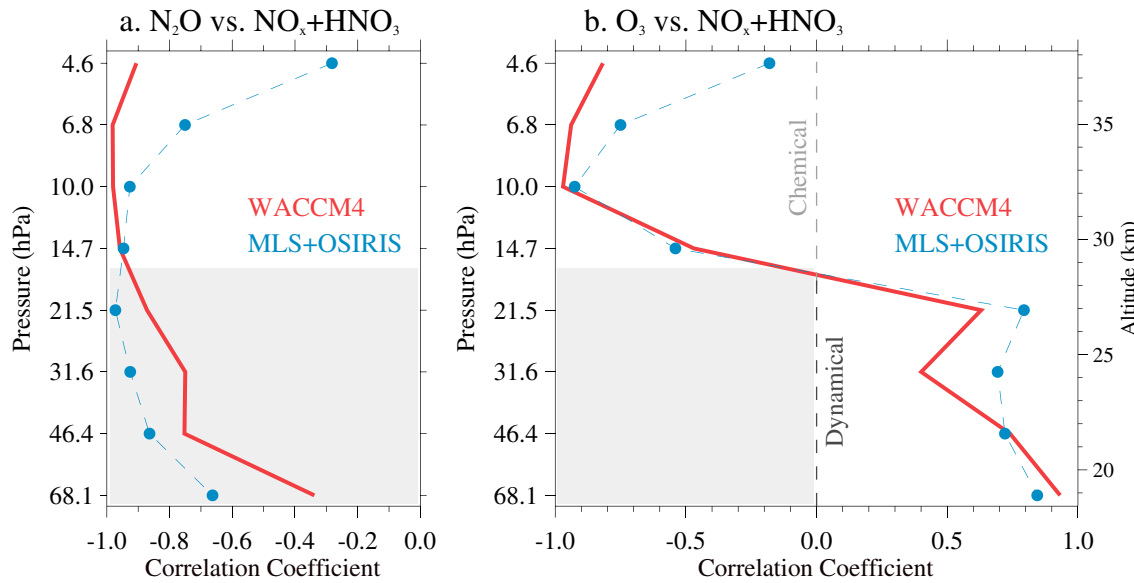


Figure 7. Vertical structures of cross-correlation coefficients between (a) N_2O and $(\text{NO}_x + \text{HNO}_3)$ and (b) O_3 and $(\text{NO}_x + \text{HNO}_3)$ in the tropics (10°S – 10°N) estimated from WACCM4 (red solid lines) and MLS + OSIRIS ($\text{HNO}_3 + \text{NO}_x^*$, blue dots) for 2005–2014. $\text{NO}_x + \text{HNO}_3$ is used as a proxy for NO_y in the tropics (see text for details).

Figures 6 and 7a). HNO_3 variations reach their maximum near ~ 15 – 22 hPa, and variations of NO_x peak above ~ 15 hPa (~ 28 km), where the time-averaged concentrations show maxima (see Figure 2). This reflects the changes in NO_y photochemical partitioning with altitude. Variations in NO_x , HNO_3 , and N_2O from WACCM4 show good agreement with satellite observations in terms of phasing with respect to the QBO, with slight differences in magnitude. MLS HNO_3 anomalies show $\sim 25\%$ larger amplitudes than those from WACCM4 near ~ 22 – 15 hPa, where time-averaged values of MLS HNO_3 mixing ratios are also larger than those from WACCM4 (Figure 2b). In contrast, amplitudes of QBO variations in both N_2O and NO_x in the upper stratosphere ($p < \sim 10$ hPa) are larger in WACCM4 than in the corresponding MLS N_2O and OSIRIS NO_x^* anomalies.

The ratios of QBO-related variations in time series of $(\text{HNO}_3/\text{N}_2\text{O})$ and $(\text{NO}_x/\text{N}_2\text{O})$ are sensitive measures of the altitude-dependent nitrogen budget in the tropical stratosphere. Altitude variations in these ratios reflect the

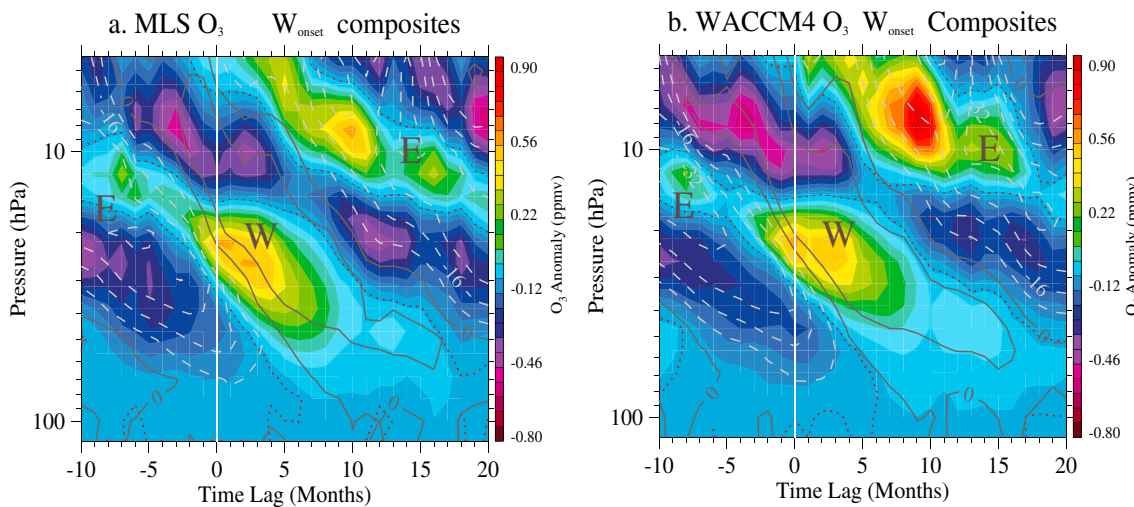


Figure 8. Pressure versus month time lag sections of QBO composite averages of O_3 averaged between 5°S and 5°N latitudes (unit: ppmv) from (a) MLS and (b) WACCM4 for 2005–2014. Monthly averaged zonal mean zonal winds from ERA-Interim (Figure 8a) and WACCM4 (Figure 8b) (unit: m s^{-1}) are overplotted as gray solid (westerly) and dashed (easterly) lines, respectively. Red dotted lines show zero contours. White solid line at zero-time lag indicates QBO westerly onset at 20 hPa.

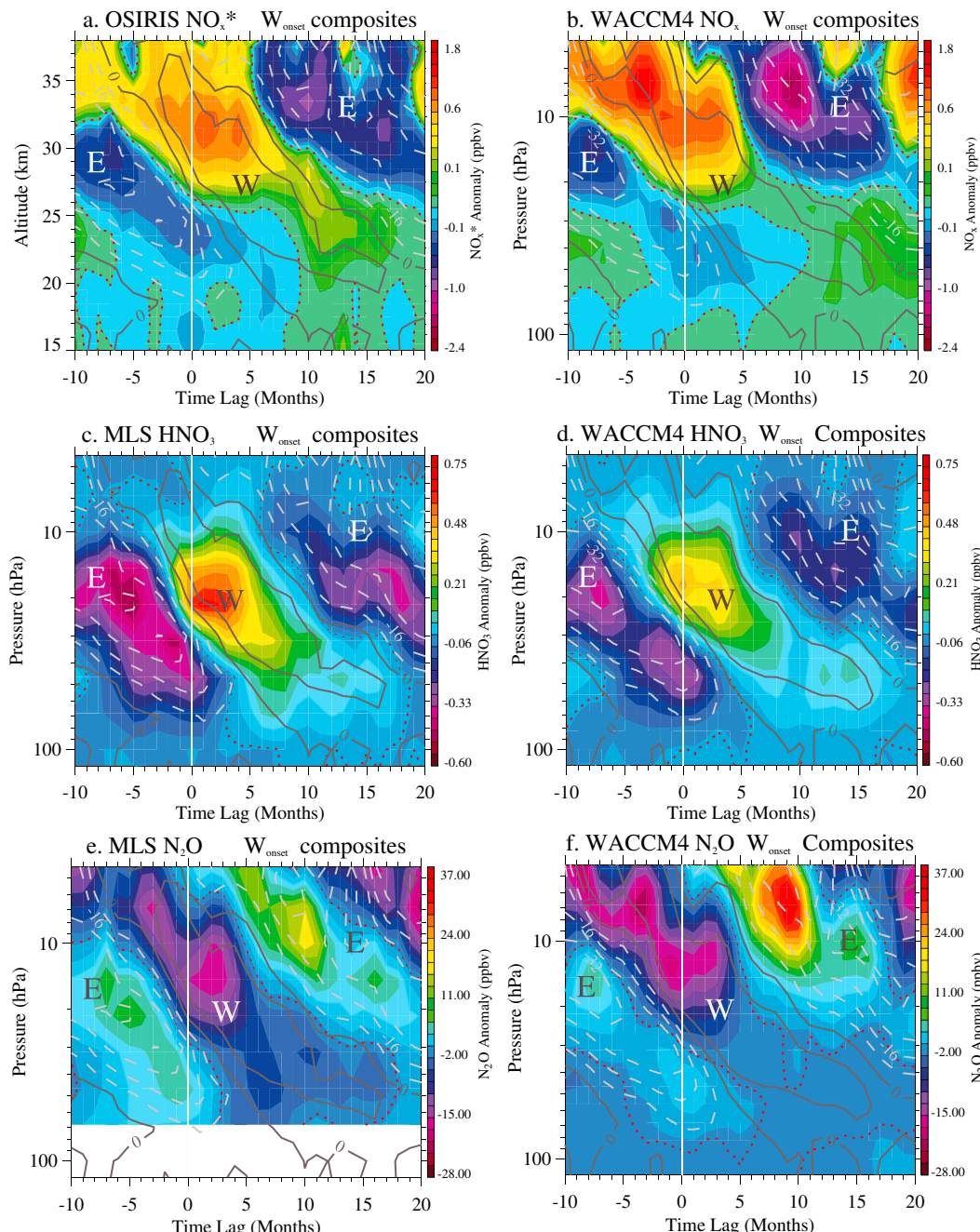


Figure 9. QBO composite averages for (a, b) NO_x , (c, d) HNO_3 , and (e, f) N_2O . Units and contour intervals are noted on each panel. Figures 9a, 9c, and 9e show results derived from OSIRIS and MLS satellite measurements, and Figures 9b, 9d, and 9f are from the WACCM4 simulations. Zonal wind composites are included, as in Figure 8.

balance between chemical partitioning and transport processes in the model. Covariations in the time series of HNO_3 , N_2O , and NO_x in the tropical stratosphere are largely influenced by the QBO. Here we make comparisons of those ratios calculated from the observations and the model using linear regression analysis. Figure 10a shows the regression coefficients of $(\text{HNO}_3/\text{N}_2\text{O})$ time series calculated from monthly mean MLS data at each pressure level (solid circles) and the same calculations from WACCM4 (solid line). The regression coefficients with respect to N_2O agree between MLS and WACCM4, and this behavior reflects the fact that both the MLS HNO_3 and N_2O anomalies show larger amplitudes than those in WACCM4 over $\sim 20\text{--}50$ hPa in Figures 9c–9f (i.e., the $\text{HNO}_3\text{--N}_2\text{O}$ biases vary in a physically consistent manner). Regression

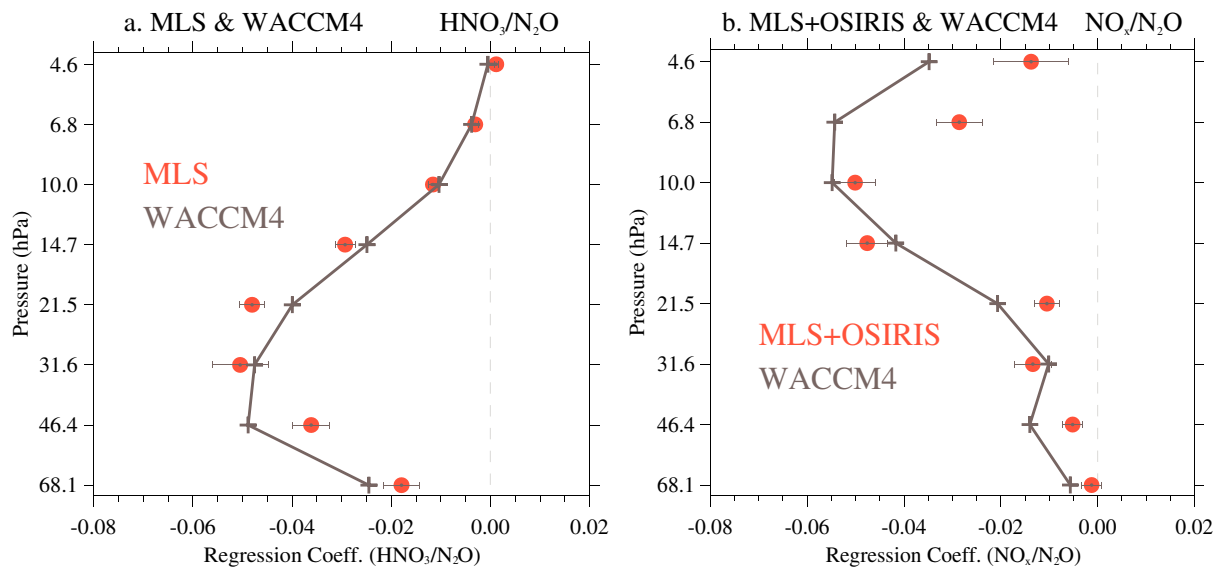


Figure 10. Altitude profiles of the ratios of (a) $(\text{HNO}_3/\text{N}_2\text{O})$ and (b) $(\text{NO}_x^*/\text{N}_2\text{O})$ derived from regression analyses at each pressure level. Results derived from satellite observations are shown as red dots (with 2 sigma statistical fit uncertainties), and results from WACCM4 are shown as the black line.

coefficients for $(\text{NO}_x/\text{N}_2\text{O})$ are shown in Figure 10b, using OSIRIS NO_x^* and MLS N_2O measurements (solid circles) and WACCM4 results (solid line). Comparison with Figure 10a reveals how the photochemical balance in NO_y shifts from HNO_3 in the lower stratosphere (~ 30 hPa) to NO_x in the upper stratosphere (~ 10 hPa). Overall, the regression coefficients of $\text{NO}_x^*/\text{N}_2\text{O}$ from OSIRIS and MLS agree with the model results between ~ 68 and 10 hPa but are systematically smaller above ~ 10 hPa. The similarity in observed versus modeled $(\text{NO}_x/\text{N}_2\text{O})$ slopes at 10 hPa is consistent with the $\sim 20\%$ WACCM4 biases in both NO_x and N_2O shown in Figure 9.

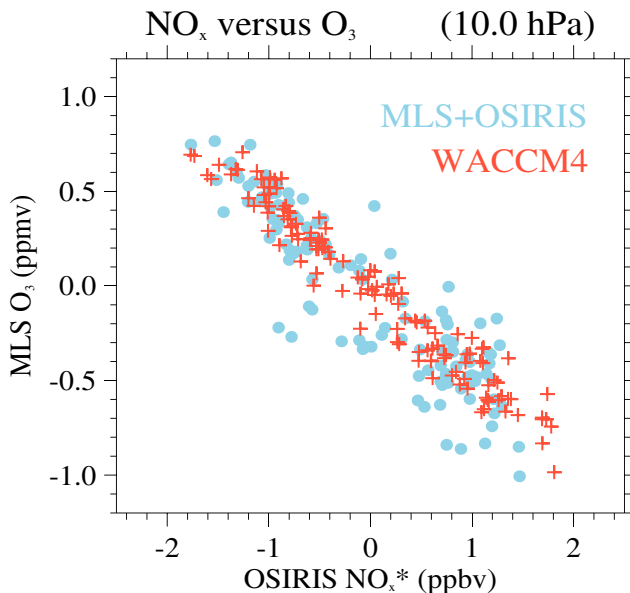


Figure 11. Scatterplots of monthly mean 10 hPa anomalies of O_3 from MLS versus NO_x^* from OSIRIS between 10°S and 10°N (solid blue dots). Corresponding results from WACCM4 NO_x and O_3 are shown as red crosses.

As noted above, variations in O_3 have strong anticorrelation with NO_x in the upper stratosphere due to NO_x control of chemical O_3 loss processes. The ratio of (O_3/NO_x) is a sensitive parameter that quantifies this relationship. Figure 11 shows tracer-tracer correlations between O_3 and NO_x^* monthly anomalies at 10 hPa derived from MLS and OSIRIS data (solid blue dots), showing strong anticorrelation. Corresponding results derived from WACCM4 are included in Figure 11 (red crosses), showing a similar compact relationship, and the derived (O_3/NO_x) slope is similar between the model and observations. This agreement suggests that upper stratospheric ozone is responding to variations in NO_x in the model in a highly realistic manner, as shown by comparison to the observations.

3.3. Global QBO Behavior

The amplitude of the QBO in zonal wind is approximately Gaussian about the equator and shows little phase dependence on latitude within the tropics (Wallace, 1973). However, the dynamical influence of the QBO extends to the extratropics via the secondary meridional circulation induced by the QBO (Gray & Chipperfield, 1990; Randel & Wu, 1996), with out-of-phase behavior between low and high latitudes (see Figure 9 of Bourassa et al., 2014). We have derived spatial patterns of the QBO signal in reactive nitrogen species from MLS (N_2O and HNO_3) and OSIRIS NO_x^* based on linear regression analysis of the equatorial zonal wind. The QBO can be best represented by the two orthogonal components, i.e., QBO1 and QBO2, constructed using the first and second leading empirical orthogonal functions of the equatorial zonal winds at seven pressure levels between 70 and 10 hPa (Wallace et al., 1993). We

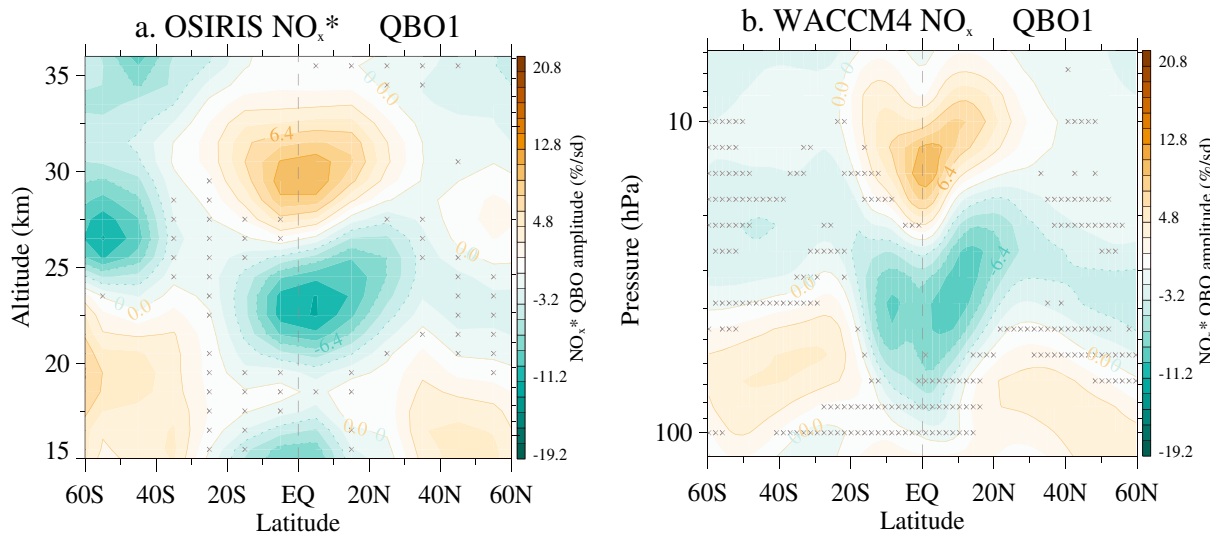


Figure 12. Latitude versus altitude sections of relative amplitudes of QBO1 regression fits for (a) OSIRIS NO_x^* and (b) WACCM4 NO_x for 2005–2014. Contours show local percent variations in NO_x associated with one standard deviation of the QBO1 reference time series. Areas with gray crosses denote statistically insignificant regions at 95% significance level.

constructed QBO1 and QBO2 components using the equatorial zonal wind observations over Singapore (Naujokat, 1986). Figure 12a shows the QBO1 regression fit for OSIRIS NO_x^* in local percentage values, i.e., divided by the local background structure to highlight variability in the lower stratosphere. The QBO2 fit reveals similar tropical and extratropical maxima, orthogonal to QBO1 (the QBO1 and QBO2 fits for O_3 , N_2O , HNO_3 , and NO_x^* are included in supporting information Figure S3). Figure 12a shows statistically significant QBO variations in OSIRIS NO_x^* in both the tropics and the extratropics, with opposite phases. The tropical QBO1 signal extends down to ~ 20 km and represents the downward propagating signal in NO_x^* as seen in Figures 5a and 9a. In addition, there are coherent QBO signals in the extratropical lower stratosphere of both hemispheres down to 15 km, linked with the extratropical component of the QBO circulation (Gray & Chipperfield, 1990). The signature of QBO1 in WACCM4 NO_x (Figure 12b) shows global structures consistent with those in OSIRIS NO_x^* , but the amplitudes are smaller. Similar QBO patterns are found both in the tropics and in the extratropics in the regression analyses results from O_3 , HNO_3 , and N_2O in MLS and WACCM4 (Figure S3), highlighting the global effects of the QBO on chemical constituents.

4. Summary and Discussion

The QBO dominates interannual variability in dynamical variables and chemical constituents in the tropical stratosphere, and variability linked to the QBO can serve as a natural experiment for quantifying chemistry-transport interactions. We have explored the QBO variations in a decade-long record of satellite measurements of stratospheric O_3 , reactive nitrogen compounds (NO_x and HNO_3), and the source gas N_2O . While the QBO signals in O_3 and NO_2 (e.g., Chipperfield & Gray, 1992; Chipperfield et al., 1994; Randel & Wu, 1996; Zawodny & McCormick, 1991) and HNO_3 (e.g., Schoeberl et al., 2008) have been analyzed previously, our study is the first to combine quantitative estimates of the key species NO_x and HNO_3 , along with the source gas N_2O . The global variations linked to the QBO also provide a tool for validating chemistry-climate model results with satellite observations. The WACCM4 model simulations used in this study are nudged to observed QBO dynamical variability which facilitates the comparisons to the observations. However, the composited tracer variability with respect to the QBO cycle (e.g., Figures 8 and 9) could be directly compared to results from a free-running model with an internally generated QBO (e.g., Hurwitz et al., 2013). Hence, this work serves both to assess satellite observations and to quantitatively evaluate global chemistry model results.

The results presented here show coherent variations among O_3 , N_2O , NO_x , and HNO_3 , for both satellite data and model simulations. Overall, the QBO variations in different species are quantitatively similar in

observations and model simulations. As an example, O_3 variations simulated in WACCM4 are in excellent overall agreement with those from MLS and OSIRIS observations (Figures 4 and 8), with larger amplitudes (up to $\sim 20\%$ difference) in model O_3 anomalies at higher altitudes (above ~ 28 km).

Both the observations and model results show QBO variations in NO_x and HNO_3 that are out of phase with respect to those of N_2O . The NO_y partitioning as a function of altitude derived from the observations is in agreement with the model results, with HNO_3 dominating below ~ 15 hPa and NO_x dominating above. This is true for both time-averaged profiles (Figure 2) and monthly anomalies (Figure 9). Furthermore, the ratios of covariations in (HNO_3/N_2O) and (NO_x/N_2O) obtained from linear regression analyses are consistent between the observations and model (Figure 10). An exception is the case of the (NO_x/N_2O) ratio at levels above 7 hPa in Figure 10b, which may signify loss of sensitivity in the OSIRIS measurements at the uppermost levels. The sensitivity of O_3 to NO_x in the upper stratosphere, quantified by the O_3 versus NO_x slope at 10 hPa (see Figure 11), is similar between model and observations. The agreement in the regression coefficients obtained from the different time series demonstrates that the satellite data, based on independent instruments using different retrieval algorithms and spectral intervals, are behaving in a physically consistent manner. These comparisons demonstrate that the reactive nitrogen budget estimated from the complementary satellite data is approximately closed for variability associated with the QBO in the stratosphere.

Comparisons with the NO_x proxy ($= NO_x^*$) are more complex than for the other species, since calculation of NO_x^* depends on both the OSIRIS observations of NO_2 (often made close to the terminator) and a photochemical box model. In spite of this highly derived nature, the overall variability of NO_x^* seems realistic and in reasonable agreement with WACCM4 results. Direct comparisons of OSIRIS and WACCM4 NO_2 are included in the supporting information. Furthermore, the global structures of NO_x variations tied to the QBO (Figure 12) are coherent between model simulations and observations, including the influence of the QBO in the extratropical lower stratosphere in both hemispheres. This is further confirmation of the quality of the OSIRIS NO_2 and derived NO_x^* proxy.

Our comparisons suggest some systematic differences between the satellite data and model results in the upper stratosphere (pressure less than ~ 10 hPa), where the QBO-linked variations in the model have $\sim 20\%$ larger amplitudes in N_2O , NO_x , and O_3 than those in the observations (see Figures 8 and 9). However, the ratios of (NO_x/N_2O) and (O_3/NO_x) are in approximate agreement between the model and observations at 10 hPa (Figures 10b and 11), suggesting that the differences occur in a physically consistent way. This behavior, along with the fact that the satellite measurements are obtained from three independent data sources (MLS N_2O , OSIRIS NO_x^* , and MLS O_3), argues against a bias in one of the data sets. Rather, it suggests possible differences in the processes in the model. Relatively larger amplitudes in QBO-related variations in the model could be explained by slower vertical transport in the upper stratosphere, which leads to enhanced NO_x generation from N_2O (i.e., larger variations in both species), and larger O_3 fluctuations tied to the resulting NO_x in the model. We leave this as an open question for further investigation.

Acknowledgments

We thank Cristen Adams for helpful discussions on the OSIRIS measurements. We thank Marta Abalos, Peter Hitchcock, and Anne Smith for discussions and comments on the manuscript. The data sets used are publicly available, the MLS data from <https://disc.sci.gsfc.nasa.gov/Aura/data holdings/MLS> and the OSIRIS data from <http://http://odin-osiris.usask.ca>. WACCM is a component of NCAR's Community Earth System Model (CESM), which is supported by the NSF and the Office of Science of the U.S. Department of Energy. Computing resources were provided by NCAR's Climate Simulation Laboratory, sponsored by NSF and other agencies. This research was enabled by the computational and storage resources of NCAR's Computational and Information Systems Laboratory (CISL). The model output and data used in this paper are listed in the references or available from the NCAR Earth System Grid. Work at the Jet Propulsion Laboratory, California Institute of Technology, was done under contract with the National Aeronautics and Space Administration. This work was partially supported by the NASA Aura Science Team funded under grant NNX14AF92G. The National Center for Atmospheric Research is operated by the University Corporation for Atmospheric Research, under sponsorship of the National Science Foundation.

References

Adams, C., Bourassa, A. E., Sofieva, V., Froidevaux, L., McLinden, C. A., Hubert, D., ... Degenstein, D. A. (2014). Assessment of Odin-OSIRIS ozone measurements from 2001 to the present using MLS, GOMOS, and ozonesondes. *Atmospheric Measurement Techniques*, 7, 49–64. <https://doi.org/10.5194/amt-7-49-2014>

Adams, C., Bourassa, A. E., McLinden, C. A., Sioris, C. E., von Clarmann, T., Funke, B., ... Degenstein, D. A. (2017). Effect of volcanic aerosol on stratospheric NO_2 and N_2O_5 from 2002–2014 as measured by Odin-OSIRIS and Envisat-MIPAS. *Atmospheric Chemistry and Physics*, 17, 8063–8080. <https://doi.org/10.5194/acp-17-8063-2017>

Baldwin, M. P., Gray, L. J., Dunkerton, T. J., Hamilton, K., Haynes, P. H., Randel, W. J., ... Takahashi, M. (2001). The quasi-biennial oscillation. *Reviews of Geophysics*, 39, 179–229. <https://doi.org/10.1029/1999RG000073>

Bourassa, A. E., McLinden, C. A., Sioris, C. E., Brohede, S., Llewellyn, E. J., & Degenstein, D. A. (2011). Fast NO_2 retrievals from Odin-OSIRIS limb scatter measurements. *Atmospheric Measurement Techniques*, 4, 965–972. <https://doi.org/10.5194/amt-4-965-2011>

Bourassa, A. E., Degenstein, D. A., Randel, W. J., Zawodny, J. M., Kyrölä, E., McLinden, C. A., ... Roth, C. Z. (2014). Trends in stratospheric ozone derived from merged SAGE II and Odin-OSIRIS satellite observations. *Atmospheric Chemistry and Physics*, 14, 6983–6994. <https://doi.org/10.5194/acp-14-6983-2014>

Brasseur, G. P., & Solomon, S. (2005). *Aeronomy of the middle atmosphere* (pp. 646). Netherlands: Springer. <https://doi.org/10.1007/1-4020-3824-0>

Brohede, S. M., Haley, C. S., McLinden, C. A., Sioris, C. E., Murtagh, D. P., Petelina, S. V., ... Gordley, L. L. (2007). Validation of Odin-OSIRIS stratospheric NO_2 profiles. *Journal of Geophysical Research*, 112, D07310. <https://doi.org/10.1029/2006JD007586>

Brohede, S., McLinden, C. A., Urban, J., Haley, C. S., Jonsson, A. I., & Murtagh, D. (2008). Odin stratospheric proxy NO_y measurements and climatology. *Atmospheric Chemistry and Physics*, 8, 5731–5754. <https://doi.org/10.5194/acp-8-5731-2008>

Bruhwiler, L. P., & Hamilton, K. (1999). A numerical simulation of the stratospheric ozone quasi-biennial oscillation using a comprehensive general circulation model. *Journal of Geophysical Research*, 104, 30,525–30,557. <https://doi.org/10.1029/1999JD900385>

Butchart, N., Scaife, A. A., Austin, J., Hare, S. H. E., & Knight, J. R. (2003). Quasi-biennial oscillation in ozone in a coupled chemistry-climate model. *Journal of Geophysical Research*, 108(D15), 4486. <https://doi.org/10.1029/2002JD003004>.

Chipperfield, M. P., & Gray, L. J. (1992). Two-dimensional model studies of the interannual variability of trace gases in the middle atmosphere. *Journal of Geophysical Research*, 97(D5), 5963–5980. <https://doi.org/10.1029/92JD00029>

Chipperfield, M. P., Gray, L. J., Kinnersley, J. S., & Zawodny, J. (1994). A two-dimensional model study of the QBO signal in SAGE II NO₂ and O₃. *Geophysical Research Letters*, 21, 589–592. <https://doi.org/10.1029/94GL00211>

Crutzen, P. J. (1971). Ozone production rates in an oxygen-hydrogen-nitrogen oxide atmosphere. *Journal of Geophysical Research*, 76, 7311–7327. <https://doi.org/10.1029/JC076i030p07311>

Dee, D. P., Uppala, S. M., Simmons, A. J., Berrisford, P., Poli, P., Kobayashi, S., ... Vitart, F. (2011). The ERA-Interim reanalysis: Configuration and performance of the data assimilation system. *Quarterly Journal of the Royal Meteorological Society*, 137, 553–597. <https://doi.org/10.1002/qj.828>

Degenstein, D. A., Llewellyn, E. J., & Lloyd, N. D. (2003). Volume emission rate tomography from a satellite platform. *Applied Optics*, 42, 1441–1450. <https://doi.org/10.1364/AO.42.001441>

Degenstein, D. A., Bourassa, A. E., Roth, C. Z., & Llewellyn, E. J. (2009). Limb scatter ozone retrieval from 10 to 60 km using a multiplicative algebraic reconstruction technique. *Atmospheric Chemistry and Physics*, 9, 6521–6529. <https://doi.org/10.5194/acp-9-6521-2009>

Fleming, E. L., Jackman, C. H., Rosenfield, J. E., & Considine, D. B. (2002). Two-dimensional model simulations of the QBO in ozone and tracers in the tropical stratosphere. *Journal of Geophysical Research*, 107(D23), 4665. <https://doi.org/10.1029/2001JD001146>

Froidevaux, L., Jiang, Y. B., Lambert, A., Livesey, N. J., Read, W. G., Waters, J. W., ... Wagner, P. A. (2008). Validation of Aura Microwave Limb Sounder stratospheric ozone measurements. *Journal of Geophysical Research*, 113, D15S20. <https://doi.org/10.1029/2007JD008771>

Gray, L. J., & Chipperfield, M. P. (1990). On the interannual variability of trace gases in the middle atmosphere. *Geophysical Research Letters*, 17, 933–936. <https://doi.org/10.1029/GL017i007p00933>

Gray, L. J., & Pyle, J. A. (1989). A two-dimensional model of the quasi-biennial oscillation of ozone. *Journal of Atmospheric Science*, 46, 203–220. [https://doi.org/10.1175/1520-0469\(1989\)046<203:ATDMOT>2.0.CO;2](https://doi.org/10.1175/1520-0469(1989)046<203:ATDMOT>2.0.CO;2)

Haley, C. S., Brohede, S. M., Sioris, C. E., Griffioen, E., Murtagh, D. P., McDade, I. C., ... Goutail, F. (2004). Retrieval of stratospheric O₃ and NO₂ profiles from Odin Optical Spectrograph and Infrared Imager System (OSIRIS) limb-scattered sunlight measurements. *Journal of Geophysical Research*, 109, D16303. <https://doi.org/10.1029/2004JD004588>

Hauchecorne, A., Bertaux, J. L., Dalaudier, F., Keckhut, P., Lemennais, P., Bekki, S., ... Saavedra de Miguel, L. (2010). Response of tropical stratospheric O₃, NO₂ and NO₃ to the equatorial quasi-biennial oscillation and to temperature as seen from GOMOS/ENVISAT. *Atmospheric Chemistry and Physics*, 10, 8873–8879. <https://doi.org/10.5194/acp-10-8873-2010>

Hommel, R., Timmreck, C., Giorgetta, M. A., & Graf, H. F. (2015). Quasi-biennial oscillation of the tropical stratospheric aerosol layer. *Atmospheric Chemistry and Physics*, 15, 5557–5584. <https://doi.org/10.5194/acp-15-5557-2015>

Hurwitz, M. M., Oman, L. D., Newman, P. A., & Song, I.-S. (2013). Net influence of an internally generated quasi-biennial oscillation on modelled stratospheric climate and chemistry. *Atmospheric Chemistry and Physics*, 13, 12,187–12,197. <https://doi.org/10.5194/acp-13-12187-2013>

Jones, A., Qin, G., Strong, K., Walker, K. A., McLinden, C. A., Toohey, M., ... Boone, C. D. (2011). A global inventory of stratospheric NO_x from ACE-FTS. *Journal of Geophysical Research*, 116, D17304. <https://doi.org/10.1029/2010JD015465>

Kinnison, D. E., Brasseur, G. P., Walters, S., Garcia, R. R., Marsh, D. R., Sassi, F., ... Simmons, A. J. (2007). Sensitivity of chemical tracers to meteorological parameters in the MOZART3 chemical transport model. *Journal of Geophysical Research*, 112, D20302. <https://doi.org/10.1029/2006JD007879>

Kistler, R., Collins, W., Saha, S., White, G., Woolen, J., Kalnay, E., ... Fiorino, M. (2001). The NCEP–NCAR 50-year reanalysis: Monthly means CD-ROM and documentation. *Bulletin of the American Meteorological Society*, 82, 247–267. [https://doi.org/10.1175/1520-0477\(2001\)082<0247:TNNYRM>2.3.CO;2](https://doi.org/10.1175/1520-0477(2001)082<0247:TNNYRM>2.3.CO;2)

Kyrölä, E., Tamminen, J., Sofieva, V., Bertaux, J. L., Hauchecorne, A., Dalaudier, F., ... Saavedra de Miguel, L. (2010). GOMOS O₃, NO₂, and NO₃ observations in 2002–2008. *Atmospheric Chemistry and Physics*, 10, 7723–7738. <https://doi.org/10.5194/acp-10-7723-2010>

Lamarque, J.-F., Emmons, L. K., Hess, P. G., Kinnison, D. E., Tilmes, S., Vitt, F., ... Tyndall, G. K. (2012). CAM-chem: Description and evaluation of interactive atmospheric chemistry in CESM. *Geoscientific Model Development*, 5, 369–411. <https://doi.org/10.5194/gmd-5-369-2012>

Lambert, A., Read, W. G., Livesey, N. J., Santee, M. L., Manney, G. L., Froidevaux, L., ... Atlas, E. (2007). Validation of the Aura Microwave Limb Sounder middle atmosphere water vapor and nitrous oxide measurements. *Journal of Geophysical Research*, 112, D24S36. <https://doi.org/10.1029/2007JD008724>

Lin, S.-J. (2004). A “vertically-Lagrangian” finite-volume dynamical core for global atmospheric models. *Monthly Weather Review*, 132, 2293–2307. [https://doi.org/10.1175/1520-0493\(2004\)132<2293:AVLFDC>2.0.CO;2](https://doi.org/10.1175/1520-0493(2004)132<2293:AVLFDC>2.0.CO;2)

Livesey, N. J., Filipiak, M. J., Froidevaux, L., Read, W. G., Lambert, A., Santee, M. L., ... Webster, C. R. (2008). Validation of Aura Microwave Limb Sounder O₃ and CO observations in the upper troposphere and lower stratosphere. *Journal of Geophysical Research*, 113, D15S02. <https://doi.org/10.1029/2007JD008805>

Livesey, N. J., Read, W. G., Wagner, P. A., Froidevaux, L., Lambert, A., Manney, G. L., ... Martinez, E. (2017). Earth Observing System (EOS) Aura Microwave Limb Sounder (MLS) version 4.2x level 2 data quality and description document, JPL D-33509 rev. A, Jet Propulsion Laboratory, California Institute of Technology, Pasadena, California, USA, 169 pp.

Llewellyn, E. J., Lloyd, N. D., Degenstein, D. A., Gattinger, R. L., Petelina, S. V., Bourassa, A. E., ... Nordh, L. (2004). The OSIRIS instrument on the Odin satellite. *Canadian Journal of Physics*, 82, 411–422. <https://doi.org/10.1139/P04-005>

Marsh, D. R., Mills, M. J., Kinnison, D. E., Lamarque, J.-F., Calvo, N., & Polvani, L. M. (2013). Climate change from 1850 to 2005 simulated in CESM1(WACCM). *J. Clim.*, 26, 7372–7391. <https://doi.org/10.1175/JCLI-D-12-005581>

McElroy, M. B., & McConnell, J. C. (1971). Nitrous oxide: A natural source of stratospheric NO. *Journal of Atmospheric Science*, 28, 1095–1098. [https://doi.org/10.1175/1520-0469\(1971\)028<1095:NOANSO>2.0.CO;2](https://doi.org/10.1175/1520-0469(1971)028<1095:NOANSO>2.0.CO;2)

McLinden, C. A., Olsen, S. C., Hannegan, B., Wild, O., Prather, M. J., & Sundet, J. (2000). Stratospheric ozone in 3-D models: A simple chemistry and the cross-tropopause flux. *Journal of Geophysical Research*, 105, 14,653–14,665. <https://doi.org/10.1029/2000JD900124>

McLinden, C. A., Bourassa, A. E., Brohede, S., Cooper, M., Degenstein, D. A., Evans, W. J. F., ... Strong, K. (2012). OSIRIS: A decade of scattered light. *Bulletin of the American Meteorological Society*, 93, 1845–1863. <https://doi.org/10.1175/BAMS-D-11-00135.1>

Morgenstern, O., Hegglin, M. I., Rozanov, E., O'Connor, F. M., Abraham, N. L., Akiyoshi, H., ... Zeng, G. (2017). Review of the global models used within the Chemistry-Climate Model Initiative (CCMI). *Geoscientific Model Development*, 10, 639–671. <https://doi.org/10.5194/gmd-10-639-2017>

Murtagh, D., Frisk, U., Merino, F., Ridal, M., Jonsson, A., Stegman, J., ... Oikarinen, L. (2002). Review: An overview of the Odin atmospheric mission. *Canadian Journal of Physics*, 80, 309–319. <https://doi.org/10.1139/P01-157>

Nagashima, T., Takahashi, M., & Hasebe, F. (1998). The first simulation of an ozone QBO in a general circulation model. *Geophysical Research Letters*, 25, 3131–3134. <https://doi.org/10.1029/98GL02213>

Naujokat, B. (1986). An update of the observed quasi-biennial oscillation of the stratospheric winds over the tropics. *Journal of Atmospheric Science*, 43, 1873–1877. [https://doi.org/10.1175/1520-0469\(1986\)043<1873:AUOTOQ>2.0.CO;2](https://doi.org/10.1175/1520-0469(1986)043<1873:AUOTOQ>2.0.CO;2)

Neale, R., Richter, J., Park, S., Lauritzen, P., Vavrus, S., Rasch, P., & Zhang, M. (2013). The mean climate of the Community Atmosphere Model (CAM4) in forced SST and fully coupled experiments. *J. Clim.*, 26, 5150–5168. <https://doi.org/10.1175/JCLI-D-12-00236.1>

Nedoluha, G. E., Siskind, D. E., Lambert, A., & Boone, C. (2015). The decrease in mid-stratospheric tropical ozone since 1991. *Atmospheric Chemistry and Physics*, 15, 4215–4224. <https://doi.org/10.5194/acp-15-4215-2015>

Prather, M. (1992). Catastrophic loss of stratospheric ozone in dense volcanic clouds. *Journal of Geophysical Research*, 97, 10,187–10,191. <https://doi.org/10.1029/92JD00845>

Punge, H. J., & Giorgetta, M. A. (2008). Net effect of the QBO in a chemistry climate model. *Atmospheric Chemistry and Physics*, 8, 6505–6525. <https://doi.org/10.5194/acp-8-6505-2008>

Randel, W. J., & Wu, F. (1996). Isolation of the ozone QBO in SAGE II data by singular-value decomposition. *Journal of Atmospheric Science*, 53, 2546–2559. [https://doi.org/10.1175/1520-0469\(1996\)053<2546:ITOQI>2.0.CO;2](https://doi.org/10.1175/1520-0469(1996)053<2546:ITOQI>2.0.CO;2)

Rienecker, M. M., Suarez, M. J., Gelaro, R., Todling, R., Bacmeister, J., Liu, E., ... Woollen, J. (2011). MERRA: NASA's Modern-Era Retrospective Analysis for Research and Applications. *Journal of Climate*, 24, 3624–3648. <https://doi.org/10.1175/JCLI-D-11-00015.1>

Salawitch, R. J., Weisenstein, D. K., Kovalenko, L. J., Sioris, C. E., Wennberg, P. O., Chance, K., ... McLinden, C. A. (2005). Sensitivity of ozone to bromine in the lower stratosphere. *Geophysical Research Letters*, 32, L05811. <https://doi.org/10.1029/2004GL021504>

Sander, S. P., Friedl, R. R., Abbott, J. P. D., Barker, J. R., Burkholder, J. B., Golden, D. M., ... Orkin, V. L. (2011). Chemical kinetics and photochemical data for use in atmospheric studies evaluation number 17 NASA panel for data evaluation, JPL Publ., 10-6, 2011.

Santee, M. L., Lambert, A., Read, W. G., Livesey, N. J., Cofield, R. E., Cuddy, D. T., ... Murtagh, D. (2007). Validation of the Aura Microwave Limb Sounder HNO₃ measurements. *Journal of Geophysical Research*, 112, D24S40. <https://doi.org/10.1029/2007JD008721>

Schoeberl, M. R., Douglass, A. R., Newman, P. A., Lait, L. R., Lary, D., Waters, M. J., ... Pumphrey, H. C. (2008). QBO and annual cycle variations in tropical lower stratosphere trace gases from HALOE and Aura MLS observations. *Journal of Geophysical Research*, 113, D05301. <https://doi.org/10.1029/2007JD008678>

Sioris, C. E., Rieger, L. A., Lloyd, N. D., Bourassa, A. E., Roth, C. Z., Degenstein, D. A., ... McLinden, C. A. (2017). Improved OSIRIS NO₂ retrieval algorithm: Description and validation. *Atmospheric Measurement Techniques*, 10, 1155–1168. <https://doi.org/10.5194/amt-10-1155-2017>

Sheese, P. E., Walker, K. A., Boone, C. D., McLinden, C. A., Bernath, P. F., Bourassa, A. E., ... Zawodny, J. M. (2006). Validation of ACE-FTS version 3.5 NO_y species profiles using correlative satellite measurements. *Atmospheric Measurement Techniques*, 9, 5781–5810. <https://doi.org/10.5194/amt-9-5781-2016>

SPARC (2010). SPARC CCMVal report on the evaluation of chemistry-climate models. In V. Eyring, T. Shepherd, & D. Waugh (Eds.), SPARC Report No. 5, WCRP-30/2010, WMO/TD - No. 40. [Available at www.sparc-climate.org/publications/sparc-reports/.]

Tegtmeier, S., Hegglin, M. I., Anderson, J., Bourassa, A., Brohede, S., Degenstein, D., ... Wang, R. H. J. (2013). SPARC Data Initiative: A comparison of ozone climatologies from international satellite limb sounders. *Journal of Geophysical Research Atmospheric*, 118, 12,229–12,247. <https://doi.org/10.1002/2013JD019877>

Tian, W., Chipperfield, M. P., Gray, L. J., & Zawodny, J. M. (2006). Quasi-biennial oscillation and tracer distributions in a coupled chemistry-climate model. *Journal of Geophysical Research*, 111, D20301. <https://doi.org/10.1029/2005JD006871>

Tilmes, S., Lamarque, J.-F., Emmons, L. K., Kinnison, D. E., Marsh, D., Garcia, R. R., ... Blake, N. (2016). Representation of the Community Earth System Model (CESM1) CAM4-Chem within the Chemistry-Climate Model Initiative. *Geoscientific Model Development*, 9, 1853–1890. <https://doi.org/10.5194/gmd-9-1853-2016>

Wallace, J. M. (1973). General circulation of the tropical lower stratosphere. *Reviews of Geophysics*, 11, 191–222. <https://doi.org/10.1029/RG011i002p00191>

Wallace, J. M., Panetta, R. L., & Estberg, J. (1993). Representation of the equatorial stratospheric quasi-biennial oscillation in EOF phase space. *Journal of Atmospheric Science*, 50, 1751–1762. [https://doi.org/10.1175/1520-0469\(1993\)050<1751:ROTESQ>2.0.CO;2](https://doi.org/10.1175/1520-0469(1993)050<1751:ROTESQ>2.0.CO;2)

Waters, J. W., Froidevaux, L., Harwood, R. S., Jarnot, R. F., Pickett, H. M., Read, W. G., ... Walch, M. J. (2006). The Earth Observing System Microwave Limb Sounder (EOS MLS) on the Aura satellite. *IEEE Transactions on Geoscience and Remote Sensing*, 44(5), 1075–1092. <https://doi.org/10.1109/TGRS.2006.873771>

Witte, J. C., Schoeberl, M. R., Douglass, A. R., & Thompson, A. M. (2008). The quasi-biennial oscillation in tropical ozone from SHADOZ and HALOE. *Atmospheric Chemistry and Physics*, 8, 3929–3936. <https://doi.org/10.5194/acp-8-3929-2008>

Zawodny, J. M., & McCormick, M. P. (1991). Stratospheric Aerosol and Gas Experiment II measurements of the quasi-biennial oscillations in ozone and nitrogen dioxide. *Journal of Geophysical Research*, 96, 9371–9377. <https://doi.org/10.1029/91JD00517>